14 Physics of Biological Systems

Conrad Escher, Hans-Werner Fink, Heinz Gross (until December 2009), Dominik Grögler, Patrick Helfenstein (since May 2009), Tatiana Latychevskaia, Jean-Nicolas Longchamp, Elvira Steinwand.

in collaboration with:
Eugen Ermantraut, Clondiag Chip Technologies (Germany), Prof. John Miao, University of California at Los Angeles (USA), Prof. Andre Geim, Manchester Centre for Mesoscience and Nanotechnology, University of Manchester (Great Britain), Dr. Ilona Müllerová, Institute of Scientific Instruments (Czech Republic), Dr. Petr Formanek, University of Dresden (Germany), Dr. Soichiro Tsujino, PSI (Switzerland).

The structural investigation of individual biological objects by employing coherent low energy electrons is the primary goal of our research. It involves holography with low energy electrons as well as coherent diffraction and is assisted by micro-structuring techniques using a focused gallium ion beam device. Our current activities are divided in the following interconnected individual projects listed below.

- **SIBMAR**
  SIBMAR stands for Structural Information of Biological Molecules at Atomic Resolution and is part of the EU "New Emerging Science and Technology" Programme. SIBMAR aims at high resolution structural information of individual biological molecules by employing coherent low energy electron waves. Partners from the Institute of Scientific Instruments Academy of Sciences of the Czech Republic in Brno, the Physics Department of the University of Manchester and the Physics-Institute of the University of Zurich are involved in SIBMAR. The overall idea is to apply holography with low energy electrons to investigate the structure of individual biological molecules. Major experimental challenges are to improve the interference resolution in electron holograms, establish methods for creating free standing thin films of Graphene transparent for low energy electrons as well as appropriate techniques to present a single protein to the coherent electron wave front. Next to these experimental issues, a second, equally important aspect for achieving high resolution structural information is the reconstruction of the electron holograms. This is achieved by back-propagating the object wave information, recorded in the hologram plane, by employing a numerical algorithm to solve the integrals governing this coherent optics problem. An international workshop entitled "Current Trends in Structural Biology at the Single Molecule Level", held in Lucerne has critically reviewed the achievements of SIBMAR and compared it to state of the art research in the high energy electron and X-ray community.

- **Electron and Ion Point Sources**
  Field Ion Microscopy and related techniques are employed for fabricating and applying novel electron and ion point sources. In collaboration with the PSI, field emitter arrays are characterized and specified for their use as bright electron sources for the XFEL (X-Ray Free Electron Laser) project.

- **Fluorescent Microscopy**
  The aim of this project is to directly observe the dynamics of single DNA molecules in liquids by video fluorescent microscopy. In combination with molecular anchoring techniques, adopted from Clondiag, we

address the energetics of a single DNA molecule. Appropriate DNA modifications for attaching fluorescent proteins to are designed by Clondiag Chip Technologies in Jena and shall serve us in our efforts to obtain structural information about proteins by electron holography.

- **Coherent Low-Energy Electron Diffraction Microscopy**
  This is a second approach, next to electron holography, of using coherent electron wave fronts for structural biology at the single molecule level. It is based on an iterative phase retrieval scheme pioneered by John Miao from the University of California at Los Angeles with whom we collaborate in this project. Both, the principle setup for holography and coherent diffraction microscopy are depicted in Fig. 14.1. In the following two selected sub-projects shall be discussed in some more detail. The first addresses the vital question of radiation damage in imaging biological molecules. The second subject is related to the coherent diffraction microscopy project which requires a coherent parallel electron beam. The latter has been realized by employing a low aberration electron lens of micrometer dimension.

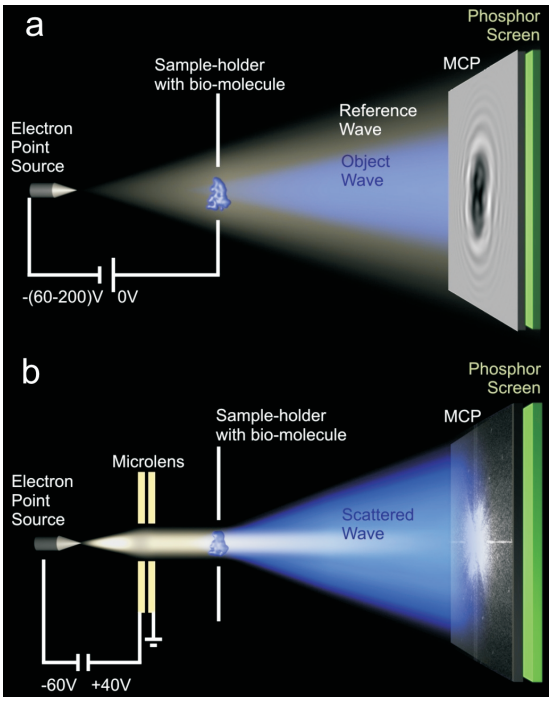

Figure 14.1: Schematic representation of the coherent electron diffraction microscope.

14.1 Non-destructive imaging of individual bio-molecules [1]

14.1.1 State of the art

Exploring the three-dimensional structure of individual biomolecules, in particular those of proteins, is the foundation for a basic understanding of bio-chemistry, molecular biology and bio-physics. Most of the protein structural information data available today have been obtained from crystallography experiments by averaging over many molecules assembled into a crystal. Despite this vast amount of available data, a strong desire for acquiring structural data from just one individual molecule is emerging for good reasons. Most of the relevant biological molecules exhibit different conformations; thus averaging does not reveal detailed structural information. Moreover, there is large quantity of proteins, in particular the important class of membrane proteins, featuring a pronounced reluctance to readily crystallize.

Due to the strong inelastic scattering of X-rays and high energy electrons there is little hope for obtaining structural information from just one single molecule by conventional X-ray or high energy electron microscopy tools. Despite recent advances in cryo-electron microscopy, especially in image processing and reconstruction, averaging over typically 10 000 images is still necessary to build up a high signal to noise ratio image with structural features finally emerging. This in turn smears

out most of the details related to conformational flexibility. The necessity for averaging is given by radiation damage inherent to the interaction with high energy electrons and limits the obtainable resolution in conventional electron microscopy to 1nanometer. In order to obtain structures of individual biological molecules at atomic resolution, new concepts and technologies are envisioned. A major effort currently underway involves the development and implementation of the X-ray Free Electron Laser (XFEL), as a source of ultra short but extremely intense X-ray pulses. The overall idea is to take advantage of the principle of inertia: by keeping the interaction time of the intense X-ray burst with the molecule of interest extremely short, the site information of the atoms is carried to the detector before the molecule has been given time to finally decompose. Unfortunately, in X-ray diffraction, inelastic scattering outweighs elastic scattering but only the latter carries information about the structure of molecules. Hence, a very large number, of the order of 10^6, diffraction patterns of identical molecules must be recorded in order to obtain structural detail at a resolution of 3 Å, even with a 10 fs X-ray pulse containing $2{\cdot}10^{12}$ photons at 1.5 Å wave length.

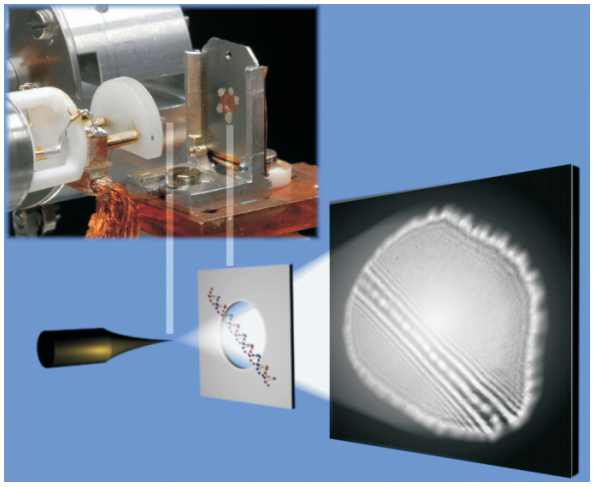

Figure 14.2: Schematic of the set-up. For exploring radiation damage effects on DNA, the molecules are exposed to coherent low energy electrons. A spherical wave emitted from a coherent electron source is scattered at DNA molecules stretched over holes in a thin film and positioned at about 1 μm beyond the source. At a 10 cm distant micro-channel-plate screen detector the interference between the elastic scattered wave (object wave) and the un-scattered wave (reference wave) produces the hologram captured by a 14 bit dynamic range CCD camera. Magnification is provided by the geometry of the set-up alone and can be adjusted by the source-sample distance. The smallest interference fringe spacing in the hologram amounts to 0.7 nm and is a measure for the achievable resolution.

14.1.2 Radiation damage in imaging DNA

In the following we show that a molecule as fragile as DNA withstands irradiation by coherent low energy electrons and remains unperturbed even after a total dose of at least 5 orders of magnitude larger than the permissible dose in X-ray or high energy electron imaging. The experimental set-up for testing radiation damage is illustrated in Fig. 14.2. DNA molecules are stretched over holes by using freeze drying technology known from cryo-microscopy. First, an array of 1 μm diameter holes in a thin carbon film is cleaned and rendered hydrophilic by UV-ozone treatment. Next, a droplet of λ-DNA solution of 2 μg/ml concentration is applied onto the carbon film. Following an incubation time of typically 10 minutes, blotting paper is used to remove excess water. The remaining thin water film is transformed into amorphous ice by rapid quenching in liquid ethane. Next, the sample is freeze-dried at -80 °C under vacuum conditions within typically 20 minutes and monitored by a mass-spectrometer above the sample. Finally, the sample is transferred into the Low Energy Electron Point Source (LEEPS)-microscope chamber for obtaining DNA electron holograms at various energies ranging from a few 10 eV up to about 300 eV.

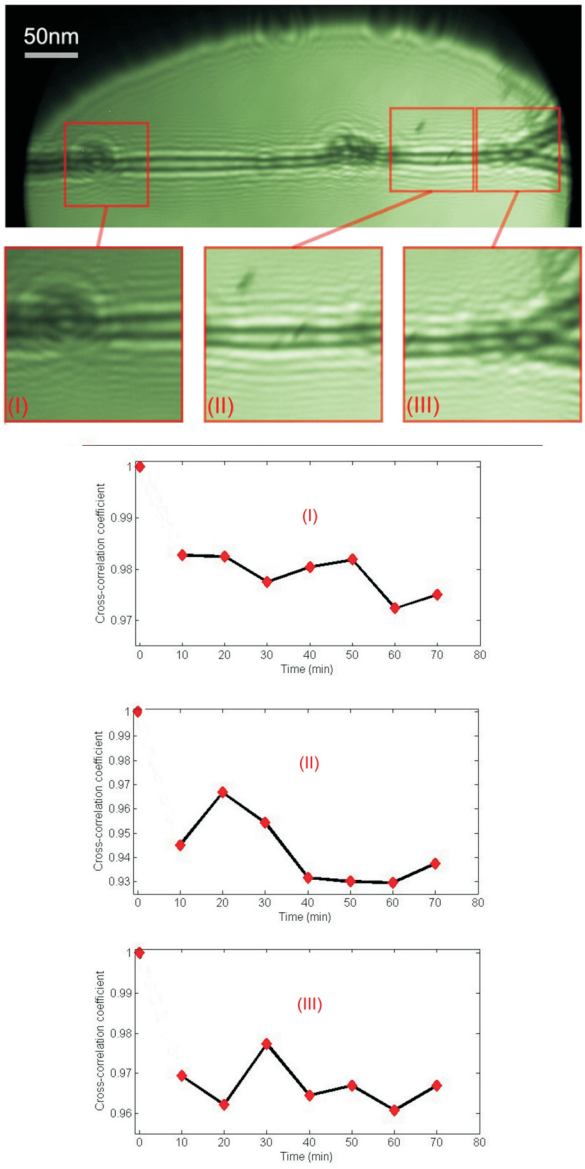

Figure 14.3: Non-destructive imaging of DNA. The low energy electron hologram of DNA molecules stretched over a hole in a thin film imaged continuously for 70 minutes using electrons of 60 eV kinetic energy and a total current of 200 nA is shown on top. Part of the rim of the 1μm diameter hole, spanning the free standing molecules, is visible at the very top of the image. Three regions of the hologram, marked in red, have been chosen to evaluate the cross-correlation function of subsequent holograms. The evolution of the cross-correlation coefficient is shown in the diagrams corresponding to the three regions.

For the holographic imaging solely the elastic scattered electrons contribute to the hologram, while the inelastic scattered electrons lead to an incoherent diffuse background at the detector level. The fraction of inelastically scattered electrons by an object can be estimated by negatively biasing the front of the detector. While there is a significant amount of inelastic scattering in imaging metals with low energy electrons, measurable inelastic scattering in imaging DNA has not been observed. This could be a first, albeit just qualitative, hint for little or no radiation damage caused by low energy electrons. To actually measure the electron dose leaving DNA molecules unperturbed, we have carried out quantitative experiments. Evidence for damage-free imaging is provided in Fig. 14.3 showing a hologram of DNA molecules subject to 60 eV electron radiation. In this experiment DNA has continuously been exposed to a 200 nA electron current for 70 minutes. A set of DNA holograms has been recorded every 10 minutes. Next, three regions in the DNA holograms have been selected, marked by red squares in Fig. 14.3. Thereafter, the cross-correlation function between the first holographic record and subsequent holograms taken at 10 min intervals have been computed for these very regions.

As is evident from Fig. 14.3, the cross-correlation coefficient varies between 0.93 and 1.0 indicating a high degree of similarity between the first and all subsequent holograms. While the fluctuation of the cross-correlation coefficient is apparent, its time dependence differs in all three DNA hologram regions. These fluctuations are due to statistical noise which varies from hologram to hologram and is attributed to the intrinsic stochastic process of field emission and to detector noise. As a consequence, the cross-correlation coefficient reaches values just below unity at best. However, there is no tendency of the cross-correlation coefficient to decay in time. In fact, the coefficient persists above 0.93 even after 70 minutes of con-

tinuous exposure. Thus, the molecule's structure remained intact during 70 minutes of exposure to 60 eV electrons. The total accumulated dose during that time amounts to 10^8 electrons/nm^2. This remarkably high electron dose certainly provides enough scattering events in a single molecule to be able to extract structural information at Ångstrom resolution. Moreover, there is nothing to be said against increasing the imaging current from 200 nA into the μA range or prolonging the exposure time. The kinetic energy of 60 eV has been chosen here because the corresponding deBroglie wave length is close to the 1.5 Å X-ray wave length used in XFEL simulations setting the boundaries for single molecule imaging. However, similar experiments as described above have also been carried out at 110 eV electron energies and quantitatively analyzed revealing the same result of no observable damage to DNA. To demonstrate that our findings depend only on electron energy but not on any particularities of our set-up, we would now like to present a control experiment, done in the same manner but at higher electron energies of 260 eV where DNA actually decomposes rapidly within a few seconds.

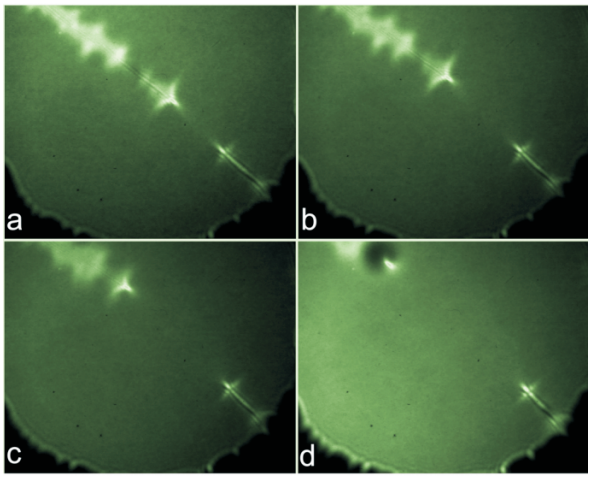

Figure 14.4: Decomposition of DNA. Control experiment showing the rapid decomposition of DNA stretched over a 1 μm diameter hole in a carbon film during imaging with 260 eV electrons.

In fact, a detailed analysis as in the non-damaging situation described above has not been possible here because of a too rapid decomposition of the molecules within the first 10 seconds of the observation process. The situation is illustrated in Figs. 14.4 and 14.5 . Again, DNA is stretched over a 1 μm diameter hole in a carbon film but now imaged with 260 eV energy electrons. Even before completing the data acquisition for the first image by the slow-scan CCD camera, the molecule had already been partly damaged as apparent in Fig. 14.4(a). Evidently the 260 eV electrons cause bond-braking in DNA. Since the DNA does not rest on a support but is free-standing, small molecular fragments created while DNA is decomposing sublimate into the vacuum. As a consequence, the remaining DNA gets shorter and shorter within a few seconds of observation.

For comparison to the non-damaging case, the evolution of the cross-correlation coefficient has also been computed and is shown in Fig. 14.5. As expected, the process of DNA decomposition is accompanied by a rapid decrease of the cross correlation coefficient between subsequent DNA images. The red bar displayed at the top of Fig. 14.5 illustrates the range of fluctuations of the cross-correlation coefficient in the non-damaging experiment.

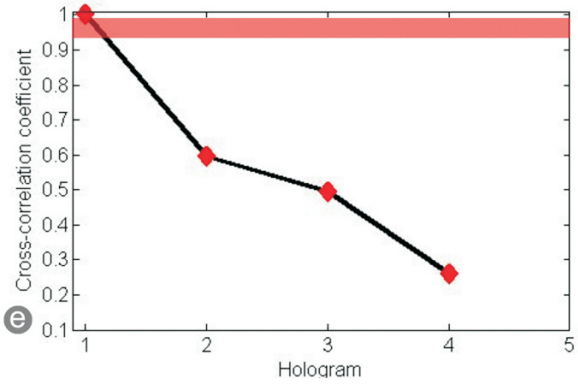

Figure 14.5: The associated change of the cross-correlation coefficient: the red bar at the top indicates the range in which this coefficient fluctuated in the non-damaging experiment with 60 eV electrons.

While 60 eV electrons apparently cause no detectable damage to DNA at all, a rapid decomposition on a 4000 times shorter time scale is observed when DNA is subject to the interaction with 260 eV electrons. We would like to point out that 60 eV kinetic energy of the imaging electron wave is not a unique value or condition for gently imaging DNA molecules. Equally non-destructive imaging conditions have empirically been found also at 115, 140, 215 and 230 eV kinetic electron energy for example. While high energy electrons in all keV kinetic energy ranges cause unavoidable damage to biological molecules, it has also been shown that very low kinetic energy electrons between 3 and 20 eV initiate strand breaks in DNA molecules. However, it is important to note that these studies suggest that there is not a simple threshold for damage, but a rather pronounced energy dependence pointing at distinct energies between 3 and 20 eV where resonance effects lead to damage.

14.1.3 Conclusion

Apparently, there are very low electron energy ranges around 10 eV, where DNA experiences rapid damage as well as higher energy resonances leading to damage at 260 eV as we have observed it and described above. But, fortunately there are also regimes in between where DNA can readily be imaged using an extremely high dose without any damage at all. The permissible dose leaving a molecule unperturbed is at least 5 orders of magnitude greater than in conventional X-rays or high energy electrons imaging, demonstrating that coherent low energy electrons are the only non-damaging Ångstrom wave lengths radiation. With coherent low energy electrons it shall thus be possible to look at truly just one entity if it comes to high resolution diffraction microscopy of individual bio molecules.

14.2 Fabrication and characterization of low-aberration micrometer-sized electron lenses [2]

14.2.1 Electron Lens Aberrations and the Scaling Concept

Back in 1936 already, Scherzer recognized that rotational symmetric static electron lenses suffer from intrinsic aberrations which have limited the resolution of conventional electron microscopes for over 50 years. These intrinsic limitations can only be overcome by using elaborate electron optical elements, like multi-pole correctors and mirrors, into the electron beam. Actually building and implementing such correctors has only recently been achieved and revolutionized modern electron microscopy design and performance. An alternative approach towards minimal aberrations relies on the concept of scaling down both electron source and lens dimensions. In scaling down the size of an electrostatic lens, the potential distribution created by the lens and with this the overall shape of the electron trajectories is conserved. Only the space in which the electron paths are shaped is changed. Thus the spherical aberration coefficient is directly proportional to the lens size. With a lens diameter of just one micrometer one assure thats the electron paths within an electron optical column deviate no more than a micrometer from the optical axes which guarantees paraxial conditions associated with minimal aberrations in all subsequent electron optical devices. While several attempts have already been undertaken in this direction, routine operation of low aberration micron-scale lenses and their application in scientific instruments are still lacking. While we routinely employ electron sources exhibiting an ultimate emission area of atomic dimension it is now a matter of scaling down a lens by about four orders of magnitude and positioning it with nanometer precision in front of the source.

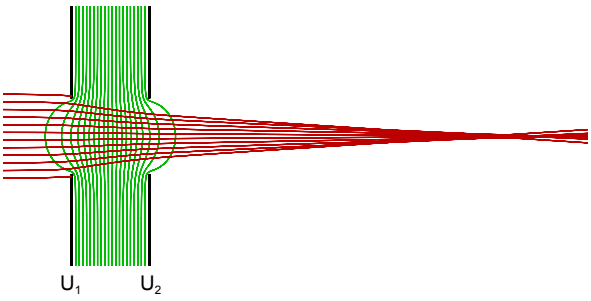

Figure 14.6: Operating principle of a two electrode aperture lens for an accelerating electrical field between the electrodes. Equipotential lines and electron trajectories have been calculated for $U_1 = 100$ V and $U_2 = 350$ V for an initial electron energy of 100 eV using a ray tracing software package.

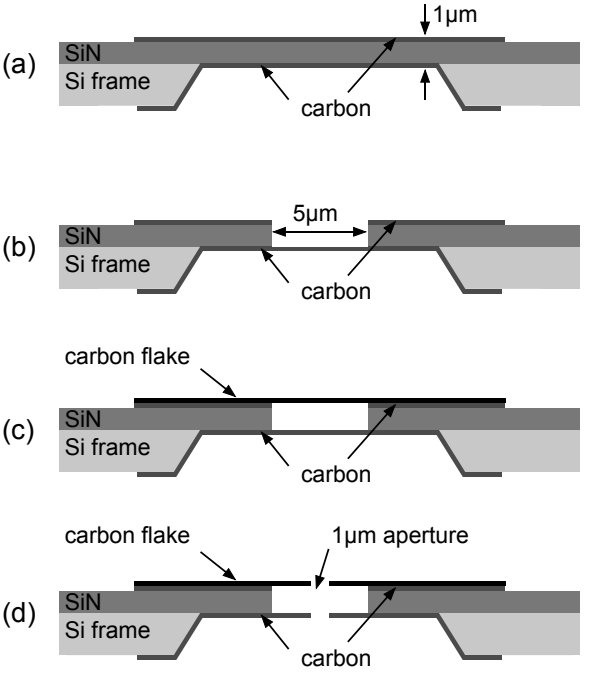

Figure 14.7: Schematic drawings of the various steps for lens fabrication.
(a) Carbon deposition on either side of a SiN membrane.
(b) Removing the upper carbon and the SiN layer in a circular 5 μm diameter region using a FIB.
(c) Covering of the structure with a carbon flake.
(d) Milling a 1 μm diameter aperture through the freestanding carbon layers using the FIB.

The simplest type of electrostatic lens consists of two parallel planar electrodes with two concentric apertures of not necessarily the same size. The electrodes must be separated by an insulating material to maintain a voltage between them, resulting in a focusing electrostatic field distribution at the apertures as illustrated in Fig. 14.6. Simulations and experiments show that the lens generates a focusing effect independent of the polarity of the applied voltage. A lens size as small as possible appears preferable in order to minimize spherical aberrations. Considering established micro-fabrication techniques and available materials, lens dimensions in the range of one micrometer appear sensible. Micrometer lens dimensions shall also ensure easy positioning of the lens in an electron-optical system using conventional nano-positioning devices based on piezo electric manipulators.

14.2.2 Lens fabrication and testing

We have developed several lens fabrication methods comprising various micro-fabrication steps, evaporation methods and materials for the insulating layers and lens electrodes. The result of all methods is a lens structure similar to the one depicted in Fig. 14.7(d) featuring a 1 μm thick insulating layer, two electrodes of several tens of nanometer thickness with one micrometer diameter apertures in them. The electrodes must be freestanding around the apertures to avoid charging effects of the insulating walls while the electron beam impinges on the lens. The fabrication of one particular type of microlens, showing good performance in terms of stability and cleanliness, will be described here in some detail. As a starting material for the fabrication we use commercially available silicon nitride (SiN) membranes of one micrometer thickness. They serve as insulating layers between the two lens electrodes and exhibit a measured breakdown voltage around 320 V, high

enough to focus a beam of electrons with kinetic energies in the range of 100 eV. The initial fabrication step consists in electron-beam evaporation of a roughly 30 nm thick layer of amorphous carbon on either side of the SiN membrane (Fig. 14.7(a)). Next, a focused gallium ion beam (FIB) is used to remove the top carbon as well as the SiN layer within a circular region of 5 μm in diameter, whereas the carbon layer at the bottom side of the structure remains unchanged (Fig. 14.7(b)). For the following process step, carbon is first evaporated onto a mica sheet. Subsequently, the carbon film is floated off onto a clean water surface and can thus be deposited onto the upper side of the structure (Fig. 14.7(c)). As the final step, a hole of 1 μm diameter is ion-milled through the freestanding parts of both carbon films (Fig. 14.7(d)). A SEM image of such final lens structure is shown in Fig. 14.8.

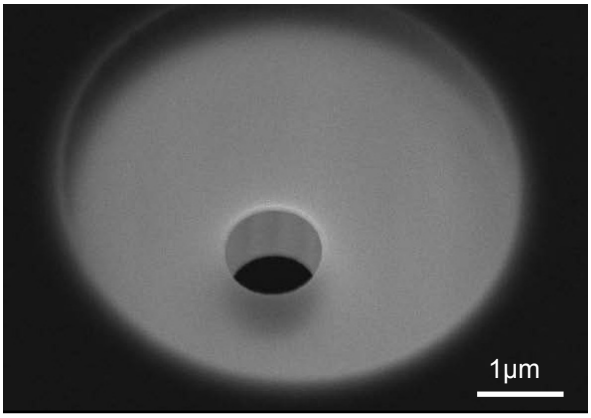

Figure 14.8: SEM image of the fabricated microlens, recorded at a tilt angle of 30 degrees. The penetration of the 12 keV electrons used in the SEM, allows recognizing the 5 μm diameter circular region where the carbon electrodes are freestanding. In this case, the lens aperture of 1 μm in diameter, is not concentric with the 5 μm region but the distance to the SiN walls is large enough to prevent charging effects when implemented as a lens.

14.2.3 Microlens operation

Lenses manufactured as described above have been tested in an ultra-high vacuum system designed for experiments with coherent low-energy electrons. A W(111) field emission tip is used as a source for a divergent electron beam of high spatial and temporal coherence. Typical emitter currents are in the 10 to 200 nA range and the kinetic energy of the electrons at the lens entrance is well below 200 eV. The electron detector consists of a microchannel plate (MCP) followed by an electroluminescent layer on the vacuum side of a fibre optic plate (FOP). At the ambient pressure side of the FOP a CCD camera collects the emitted light. The detector resolution has been measured to be around 120 μm. A dedicated holder allowing for rapid vacuum transfer of microlenses fixes the position of the lens (Figs. 14.9 and 14.10). The distance between lens and detector amounts to 75 mm. The electron source is mounted onto an x-y-z piezo stage for precise alignment with the lens aperture. For the experiments described here, the source to lens distance varied between 5 and 30 μm, leading to kinetic energies of the electrons at the lens entrance between 60 and 150 eV.

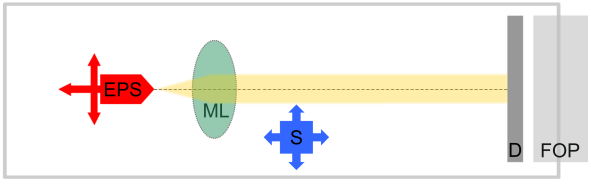

Figure 14.9: Schematic of the experimental UHV setup. The electron point source (EPS) is mounted onto an x-y-z piezo stage for nanometer precision alignment with the centre of the 1 micrometer diameter aperture of the microlens (ML). Beyond the microlens, a second x-y-z piezo stage carries the sample holder (S) to be moved into the beam. The beam profile is measured at a detector (D) placed at 75 mm beyond the lens. A fiber optic plate (FOP) transfers the image from the UHV to the ambient pressure side where it is captured by a CCD camera.

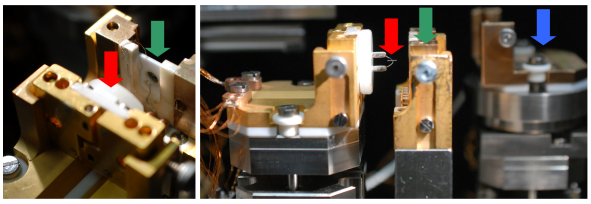

Figure 14.10: Two views into the experimental chamber showing the electron point source (red arrow), the microlens holder (green arrow) and the sample holder (blue arrow).

If the lens electrodes are at ground potential and a negative voltage is applied to the emitter tip, a projection image of the second lens aperture is visible at the screen. Its magnification can be varied by changing the source-lens distance. Examples of such electron projection images are shown in Fig. 14.11(a) and (e). Once a voltage is applied between the two lens electrodes, a focusing effect is observed. To ensure a field-free region beyond the lens, the second electrode is kept at ground potential. The voltage applied at the first lens electrode is varied together with the voltage at the emitter tip to keep the kinetic energy of the electrons at the lens entrance and the emission current constant. The voltage polarity at the first electrode can be chosen to either decelerate or accelerate the electrons when passing the lens. The effect of the lens is illustrated in Fig. 14.11 for both modes of operation. While increasing the voltage between the two lens electrodes, one first observes that the projection image of the lens aperture at the screen decreases (Fig. 14.11(b) and (f)). A further increase of the lens voltage reduces the divergence angle more and more until the electrons form a minimal spot at the detector (Fig. 14.11(c) and (g)). With still higher lens voltage, a crossover located between lens and detector is achieved (Fig. 14.11(d) and (h)). The distance between lens and crossover can even get smaller than the source-lens distance, resulting in an enlarged divergence angle of the beam as it is the case in illustrated in Fig. 14.11(d).

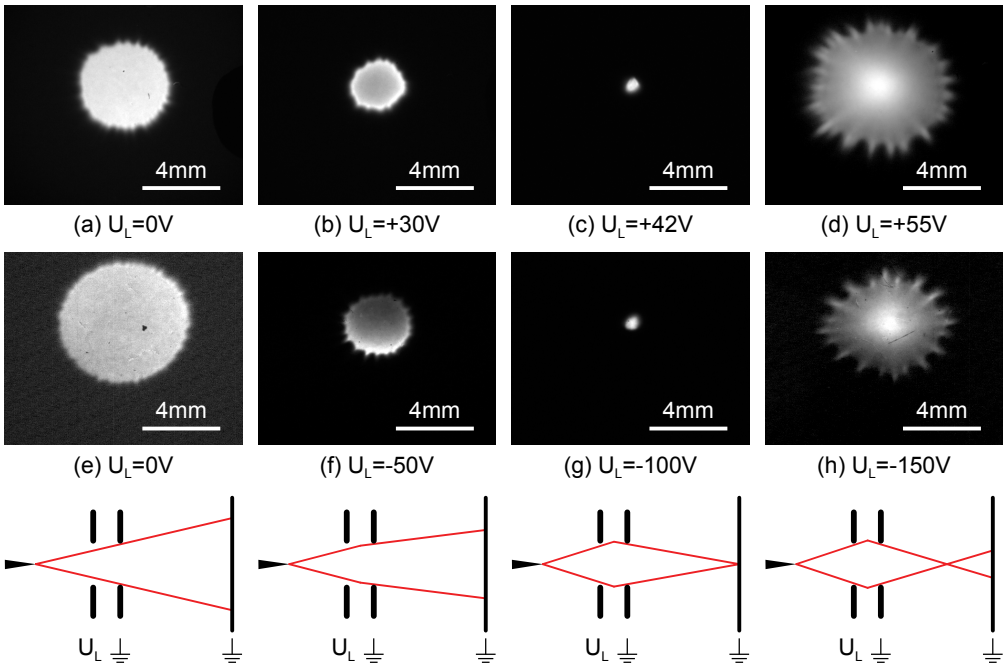

Figure 14.11: Focusing series of decelerating (top) and accelerating (middle) mode of the lens with corresponding focusing situations (bottom). The distance between virtual electron source and the first lens electrode amounts to 16 μm for the mode with a kinetic energy of 93 eV respectively 95 eV at the lens entrance.

14.2.4 Microlens performance and its aberration coefficients

To evaluate whether down-scaling of spherical aberrations by scaling down the size of the lens could actually be realized, the magnitude of spherical aberrations must be determined. Two quantities which are directly related to spherical aberrations are measured. In a second step they are compared to values obtained from ray tracing simulations assuming an idealized lens deteriorated only by intrinsic spherical aberrations. The order of magnitude of the spherical aberration coefficients de facto realized in the experiments can thus be deduced.

An experimentally easily accessible quantity is the image size of the electron source in the plane of the electron detector which is the smallest achievable spot size at the detector. As the distance from the lens to the detector plane is large compared to the diameter of the lens aperture, a minimal spot size at the detector is achieved when the beam leaves the lens almost parallel. Instead of determining spherical aberrations from the size of the spot obtained when a parallel incoming beam is focused, we do it the other way round. We instead measure the minimal achievable divergence when collimating a beam emitted by an almost perfect point source. Thus, the minimal spot size at the detector is directly related to the spherical aberrations of the lens. The minimal achievable spot size was measured for the decelerating mode of the lens. Each measurement started with recording a projection image of the lens aperture. This allowed determining the distance between the virtual electron source and the first lens aperture. Next, the lens voltage was adjusted for obtaining a minimal spot at the distant detector. The mean diameter of the minimal spot and the projection image was determined by fitting an ellipse to the contour of the half maximum of the images. It turns out, that the average spot size at the detector varies from 0.5 to 1.1 mm, measured with a detector resolution of 120 μm. Thus, assuming a Gaussian spot profile the broadening of the spot imposed by the finite detector resolution amounts to less than 3% and will not be accounted for in the following analysis. In addition to spherical aberrations there are several other intrinsic effects contributing to the size of the spot visible at the detector, namely chromatic aberrations, diffraction of the beam at the lens aperture and finite source size. For an estimation of chromatic aberrations the energy spread of 0.1 % of the electrons must be taken into account as well as the stability of the lens voltage. Ray tracing simulations showed that this leads to an enlargement of the spot size at the detector by about 15 μm. We estimated the influence of diffraction for the decelerating mode of the lens, by assuming a parallel beam being diffracted by the second aperture of the lens. This leads to a width of the central maximum of the diffraction pattern of 15 μm for 50 eV electrons. The magnified image of the virtual electron source contributes with less than 8 μm to the spot size, as the size of the virtual electron source is well below 1 nm; in fact it has been measured to be of atomic dimension. We can thus conclude that chromatic aberrations, diffraction at the lens aperture and finite source size are negligible contributions to the minimal spot size at the detector.

A more direct way to determine aberrations is to measure the beam diameter in a plane much closer to the lens than the 75 mm distant detector plane. This has been done by scanning a sharp edge perpendicular to the optical axis through the beam. The beam diameter in the plane of the edge is given by the displacement of the edge from the position where all electrons are blocked to the po-

sition where all electrons pass the edge. We fabricated such sharp edge by ion-milling a rectangular window into a 20 nm thick carbon foil, opaque for low-energy electrons. The sample was mounted onto a movable piezo-stage (see also Figs. 14.9 and 14.10) and the window was positioned into the electron beam 200 μm beyond the lens. Precise motion of the edge perpendicular to the optical axis is realized with a piezo-scanner exhibiting a scan-range of 4 μm. While moving the sample with a scan speed of typically 800 nm/s, the total intensity at the detector is recorded. The lens voltage is then adjusted for the steepest slope in the intensity versus edge position profile while repeatedly scanning through the beam.

Calculation of electrostatic fields and electron trajectories are done with the SIMION 8.0 software package to solve the Laplace equation using the finite element method. The lens is modeled as two planar electrodes separated by 1 μm and exhibiting concentric apertures of 1 μm in diameter with field-free regions on either side of the lens. Cylindrical symmetry reduces the computational effort since the Laplace equation must only be solved in two dimensions. The electrical field distributions are calculated on a 15000x1000 array with a grid size of 5 nm. Ray tracing was done with a fourth order Runge-Kutta algorithm implemented in SIMION.

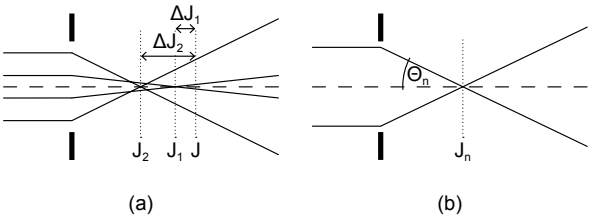

Figure 14.12: (a) Schematic drawing showing two rays with different initial distances from the optical axis which are focused at different positions J_1 and J_2. The paraxial focus is denoted as J. ΔJ_1 and ΔJ_2 are called the longitudinal spherical aberrations of the two rays. (b) The position of the focus J_n depends on the semi angular aperture Θ_n of the ray.

Spherical aberrations cause paraxial and marginal rays to be focused at different po sitions, as illustrated in Fig. 14.12. The distance between the paraxial focus J and the focus J_n of a ray passing the lens at a larger distance from the optical axis is called the longitudinal spherical aberration ΔJ_n of the ray, see Fig. 14.12(a) for denotation. In the case of a parallel incoming beam, the longitudinal spherical aberration of a ray ΔJ_n can be expressed as a power series of the ray's semi angular aperture Θ_n (see also Fig. 14.12(b)). As ΔJ_n is a symmetric function of Θ_n, the odd power terms vanish which leads to:

$$\Delta J_n = C_s \Theta_n^2 + c_4 \Theta_n^4 + c_6 \Theta_n^6 + ...,$$

Calculations were carried out for a parallel incident ray, both for the accelerating as well as for the decelerating mode of the lens. For this, a parallel beam of about 100 electrons has been generated, such that the lens aperture is completely filled. For each particle, the focus position J_n and the elevation angle Θ_n are computed. The position of the paraxial focus J is approximated by the focus of the ray with an initial distance to the optical axis of 5 nm. In this way, the longitudinal aberration $\Delta J_n = J - J_n$ is determined for each particle. A polynomial of sixth order is then fitted to the values $\Delta J_n(\Theta_n)$, yielding the primary aberration coefficient C_s. The described procedure has been applied to a series of lens voltages for the decelerating and accelerating mode respectively. In the following, voltages are always taken relative to the potential where the kinetic energy of the electrons is zero. Thus, the lens is completely described by its geometry and the voltages ratio between the two electrodes. The dependence of C_s on the voltage ratio for the accelerating and decelerating mode are shown in Fig. 14.13 for voltage ratios related to realistic experimentally accessible values. Aberration coefficients C_s are in the range of millimeters per square radian for both modes and decrease with increasing focusing strength of the lens. An ap-

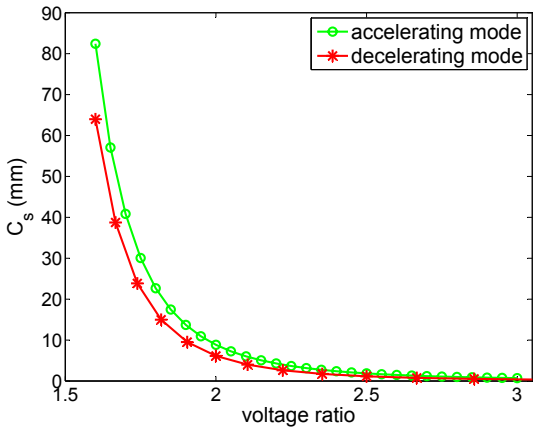

Figure 14.13: Primary aberration coefficient C_s as a function of the voltage ratio for the decelerating and accelerating mode of the lens.

proximate value for the lateral size of the focal spot d_s could be calculated using the relation $d_s = 0.5 C_s \Theta^3$. For a crossover some tens of micrometers away from the lens, this yields a spot size of several tens of nanometers.

For comparison with experimental values the size of the image of the electron source was calculated in the detector plane 75 mm beyond the lens and in the plane located 200 μm beyond the lens. As the main contribution to the finite spot size in a plane distant to the lens is due to spherical aberrations, other factors influencing the spot size, as there are chromatic aberrations, finite source size and diffraction effects, were neglected. A monochromatic point source was thus assumed for the simulations. Since typical experimental tip to lens distances are larger than 5 μm, the electrostatic field near the first lens-aperture and the strong field close to the field emission tip the apex do not influence each other, so that they can be treated as two separated electron-optical components. The electron trajectories in the immediate vicinity of the field emission tip are slightly curved as most of the potential drops in front of the tip. However, further away from the tip, at the position of the lens, the trajectories are straight lines. At the lens entrance they seem to emanate from a virtual source located a short distance behind the physical tip apex. There is thus no need to include the field emission tip in the electrode array. Instead, the region at the entrance side of the lens can be assumed as field-free. Electrons originate at a point corresponding to the position of the virtual source and propagate straight with given kinetic energy and divergence angle towards the lens. As the region behind the lens is field-free, the beam radius in the planes of interest up to the 75 mm distant detector is calculated by extrapolating the trajectories. In accordance with experimental conditions, a sufficiently large divergence angle was selected to ensure that the electrons completely fill the lens aperture. The distance between subsequent electrons in the plane of the lens aperture was set as close as possible, that is to one grid unit corresponding to 5 nm. For several distances between electron source and first lens-aperture the spot radius in the plane under consideration was calculated for a set of various lens voltages. In this way, the minimal possible spot radius was computed as a function of source-lens distance for both planes evaluated in the experiments, which is at 75 mm and 200 μm beyond the microlens.

Measured spot sizes at the detector as a function of source-lens distance are depicted in Fig. 14.14, together with the corresponding simulated values. Simulations predict a minimal spot size at the detector between 0.2 and 1.1 mm in diameter for source-lens distances ranging from 5 to 30 μm. As expected, the increase of the divergence angle with decreasing source-lens distance leads to a larger spot size. The simulated values exhibit some fluctuations which are due to the limited precision in the determination of the lens-voltage required to form a minimal spot. Together with the simulations, two series of experimental measurements of the spot size at the detector are also plotted in Fig. 14.14. For series 1 several measurements were carried out with one and the same lens, fabricated in the manner described above. In contrast to

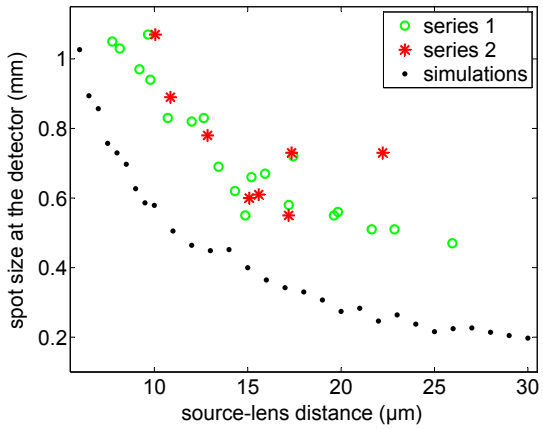

Figure 14.14: Simulated and experimental values for the minimal spot size at the detector. Series 1 was obtained with a sinle lens. Series 2 correspond to measurements with eight different lenses.

this, the eight data points of series 2 were obtained from measurements with eight different microlenses. Some of those lenses have been produced by methods different from the one described here; however all of them exhibit the same geometry. The measured values for the minimal spot size at the detector show the predicted dependency. The experimental data points however are shifted by 0.3 mm towards higher values compared to the simulated ones. The measured spot sizes assume values between 0.5 and 1 mm corresponding to a divergence angle of the collimated beam between just 6 and 14 mrad. The experimental values of series 2 obtained with different lenses exhibit similar characteristics. This implies that microlenses with comparable quality can now routinely be fabricated in a reproducible way. Moreover, as different lens fabrication methods result in similar lens performances, they appear to be equivalent with respect to the focusing properties of the lenses.

The simulated spot-sizes in the plane 200 μm beyond the lens vary from 3 μm diameter for a source-lens distance of 6 μm down to 0.6 μm diameter for a source-lens distance of 30 μm. Experimental values were obtained

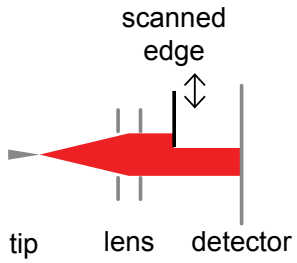

Figure 14.15: To measure the beam diameter 200 μm beyond the lens, a micro-machined edge is scanned through the beam while the total intensity at the screen is recorded.

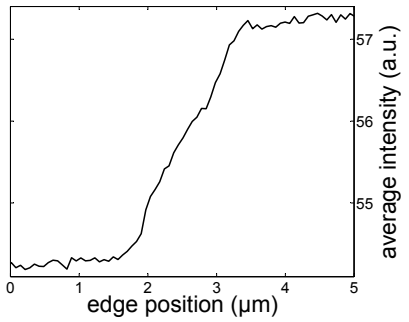

Figure 14.16: Intensity versus the edge position for a source-lens distance of 14 μm. A beam diameter of 1.8 μm is deduced.

as described above (see Fig. 14.15). For a source-lens distance of 14 μm and 92 eV electrons at the lens entrance, a lens-voltage of 48 V was found to generate a minimal spot. In Fig. 14.16, the total intensity at the screen, averaged over all pixels of the CCD chip, is plotted versus the position of the edge while moved perpendicular to the beam with a scan speed of 800 nm/s. From the intensity profile, a beam diameter of 1.8 μm has been derived. Corresponding simulations assuming identical conditions reveal a value of 1.2 μm. As the distance of 200 μm is still large compared to the 1 μm diameter of the lens apertures, focusing of the beam towards this plane is impossible. Instead, the beam diameter is minimal, when the beam leaves the lens as parallel as possible. Thus, the focusing conditions for a minimal beam diameter are just as

in the case of a 75 mm distant detector as described and discussed above. In fact, the values for the beam divergence angle obtained by the two methods are in very good agreement; they amount to 9 mrad for a source-lens distance of 14 μm.

14.2.5 Conclusions

We could show that electrostatic lenses of micrometer dimensions can readily be fabricated and exhibit reproducible performance. Comparisons with ray tracing simulations show that the concept of scaling down spherical aberrations by decreasing lens dimensions can in fact be realized. Effects like misalignment of tip and lens, residual vibrations and ac-magnetic fields, deviations from perfect lens-symmetry and contaminations of the apertures have not been considered at all in our simulations. Therefore, the experimental values for the spot size are somewhat larger than the values predicted by simulations. Although these effects do reduce lens performance slightly, their magnitude turns out to be small compared to the achieved reduction of spherical aberrations by down-scaling lens dimensions. As a result, a simple micrometer-sized lens exhibits aberration coefficients comparable to those of high performance objective lenses found in modern electron microscopes. While the bare number of the aberration coefficient is just one aspect, an even more important feature of the scaling concept is the fact that the electron beam is always kept close to the optical axes. The coherent divergent beam originating from the electron point source is modified early on by the lens and thus never spreads out to macroscopic dimensions. The nearly parallel beam beyond the microlens deviates less than one micrometer from the optical axes at a distance of 200 micrometer beyond the lens. This implies that all following electron optical devices, as an objective lens for example, perceive a micron dimension paraxial electron beam with a broadening of just 10 mrad. No beam limiting aperture to improve resolution but decrease brightness at the same time would consequently be needed for an objective lens positioned beyond the microlens. Furthermore, since a coherent electron point source is combined with the microlens, imaging technologies relying on the wave character of electrons, like holography or coherent diffraction, appear feasible. The atomic dimension emission area of the source in combination with the microlens appears to also be favourable when it comes to creating a focus by means of an objective lens. Since the focus is nothing but the image of the primary source, there would be no need to obtain a demagnified image of the primary source. A sharp focused beam could thus be obtained and directed towards a sample placed at a convenient large working distance. In having shown the performance of such microlenses, we now expect and hope for a number of exciting applications in imaging with coherent low-energy electrons.

[1] M. Germann, T. Latychevskaia, C. Escher, H.-W. Fink, Phys. Rev. Lett. 104 (2010) 095501, and references therein.

[2] E. Steinwand, J.-N. Longchamp, H.-W. Fink, Ultramicroscopy (2010), in press.